Electronic Supplementary Material (ESI) for Soft Matter.


# Supporting Information: The concentration and temperature dependent interactions and state diagram of dispersions of copolymer microgels

José Ruiz-Franco[a,b,c], Rodrigo Rivas-Barbosa[b,d], Mayra A. Lara-Peña[d,e], J. R. Villanueva-Valencia[d], Angel Licea-Claverie[e], Emanuela Zaccarelli*[a,b], and Marco Laurati*[f]

[a]CNR Institute of Complex Systems, Uos Sapienza, Piazzale Aldo Moro 2, 00185, Roma, Italy
[b]Department of Physics, Sapienza University of Rome, Piazzale Aldo Moro 2, 00185 Roma, Italy
[c]Physical Chemistry and Soft Matter, Wageningen University & Research,, Stippeneng 4, 6708WE Wageningen, The Netherlands
[d]División de Ciencias e Ingenierías, Universidad de Guanajuato, Lomas del Bosque 103, 37150 León, Mexico
[e]Centro de Graduados e Investigación en Química del Tecnológico Nacional de México/Instituto Tecnológico de Tijuana, 22500 Tijuana, Mexico
[f]Dipartimento di Chimica and CSGI, Università di Firenze, 50019 Sesto Fiorentino, Italy

## SI. NMR CHARACTERIZATION

The content of PEGMA and PNIPAM in the nanogels was evaluated by proton nuclear magnetic resonance spectroscopy ($^1$H-NMR) by using a Varian Mercury, 200 MHz equipment. Dried microgels of known weight (0.1 g) were dispersed in 2 mL of deuterated chloroform (CDCl3) by using an ultrasonic bath for 60 min keeping the dispersion cold. Fig. S1 shows the spectrum obtained from the measurement, indicating a final weight fraction of 66:34.

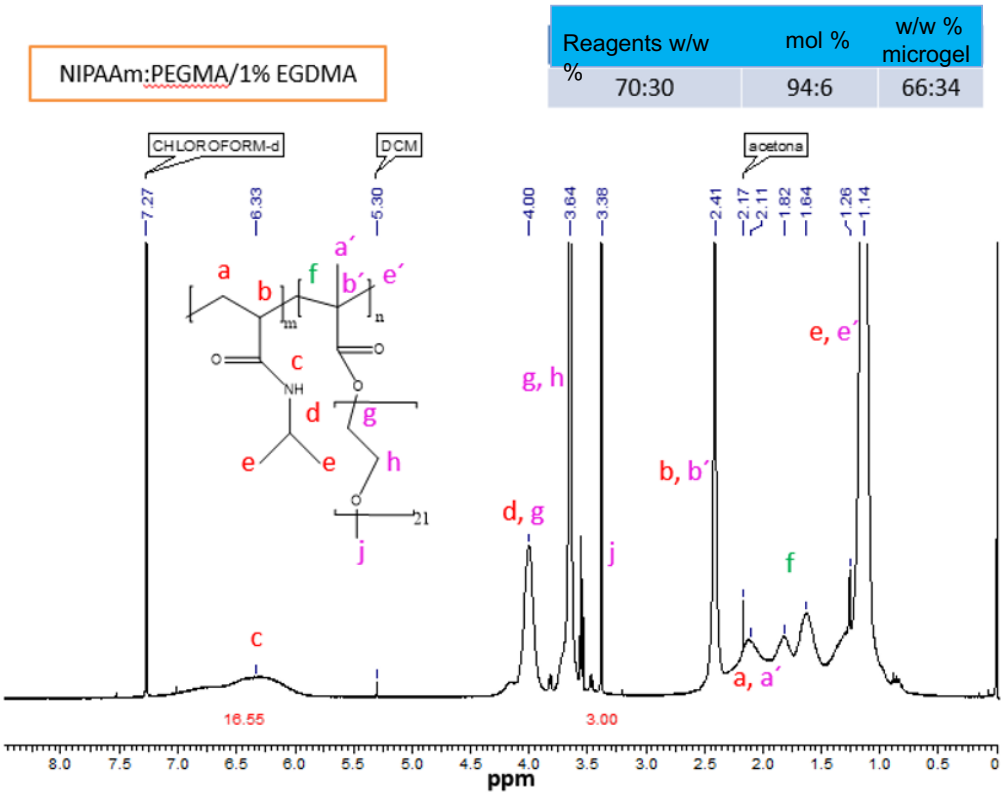


Figure S1: $^1$H-NMR Spectrum of PNIPAM-PEGMA microgels with nominla weight fractions 70:30. Analysis of the spectrum reveals a final composition of 66:34.

## SII. PARTICLE SIZE DISTRIBUTION FROM DYNAMIC LIGHT SCATTERING

Fig. S2 reports the experimental particle size distribution obtained by Dynamic Light Scattering (DLS) measurements of a dilute (c = 0.1% w/w) suspension of PNIPAM-PEGMA microgels. A Zetasizer Nano ZS (ZEN3690; Malvern Instruments, Miami, FL) equipped with a red laser of 630 nm was used for the measurements, that were performed at a scattering angle of 90°. The size distribution was obtained by using CONTIN analysis. The reported hydrodynamic diameters ($2R_h$) were calculated using the Stokes–Einstein Equation for spheres.

## SIII. SEM CHARACTERIZATION

SEM imaging of the microgels was performed on a FEG-SEM ΣIGMA (Carl Zeiss, Germany) using an acceleration potential of 2 kV and a working distance of about 3 mm. The sample was prepared by drying a droplet of a c = 0.2% w/w microgel solution onto a fragment of a cleaned silicon wafer. The image shows an exemplary collapsed, dehydrated particle, presenting a relatively uniform intensity distribution, without any clear evidence of a core-shell structure.

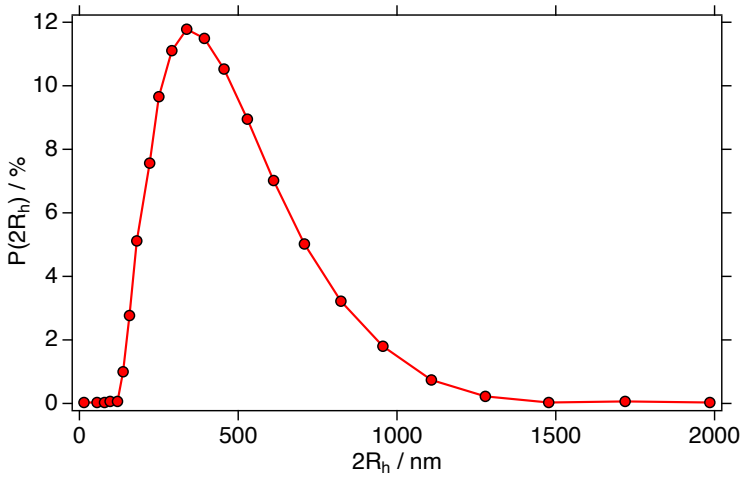

Figure S2: Particle size distribution obtained from Dynamic Light Scattering measurements at T = 20 °C.

Figure S3: SEM image of a PNIPAM-PEGMA particle in the collapsed, dehydrated state.

## SIV. SANS: FIT RESULTS OBTAINED AT T = 20 AND 30 °C FOR THE STAR POLYMER POTENTIAL

Fig. S4 shows the scattering intensities measured for samples with different effective packing fractions $\phi_{\text{eff}}$ at T = 20 and 30 °C, and fit curves obtained by modeling the form factor according to Eq. 6 of the main article, in which the particle form factor $P(Q)$ was modeled using Eq. 7 of the main article and the structure factor $S(Q)$ was calculated by solving the Ornstein-Zernike equation for the star polymer potential of Eq. 9 of the main article. The modeling of the experimental data is satisfactory for all $\phi_{\text{eff}}$. Fitted parameters can be found in Table S2.

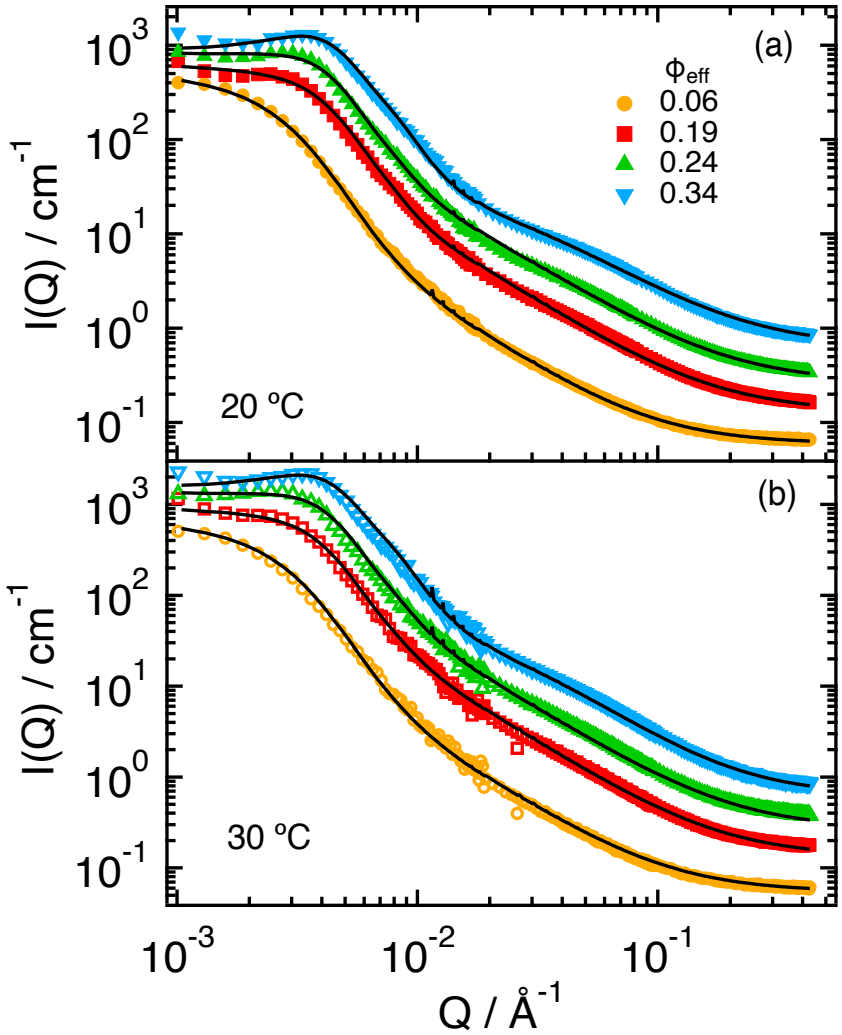


Figure S4: SANS scattering intensities $I(Q)$ for $\phi_{\text{eff}} = 0.06$, 0.19, 0.24, 0.34, as indicated, and T = 20 (a) and 30 °C (b). Lines represent fits in which the structure factor $S(Q)$ has been calculated by modeling the interactions through the star polymer potential with $f = 500$. Data and fits for $\phi_{\text{eff}} = 0.19$, 0.24 and 0.34 were vertically shifted by factors 2, 4, 8, respectively, for better visualization.

## SV. EXPERIMENTAL FIT PARAMETERS: EFFECTIVE POTENTIAL FROM SIMULATIONS

We report in Table S1 the parameters of the fits obtained from the modeling of the experimental data at T = 20, 30 and 40 °C using Eq. 6 of the main article, in which the structure factor was calculated using the effective potential obtained from simulations. The corresponding error of each parameter is also reported.

| T = 20 °C | | | | |
|---|---|---|---|---|
| $\phi_{\text{eff}}$ | 0.06 | 0.19 | 0.24 | 0.34 |
| $A_1$ (cm$^{-1}$) | 590 ± 10 | 530 ± 10 | 430 ± 8 | 310 ± 6 |
| $A_2$ (cm$^{-1}$) | 12 ± 1 | 23 ± 1 | 12 ± 1 | 4.8 ± 0.3 |
| $\xi_1$ (Å) | 220 ± 5 | 192 ± 4 | 115 ± 3 | 50 ± 2 |
| $\mu_1$ (Å) | 0.66 ± 0.02 | 0.66 ± 0.02 | 0.66 ± 0.02 | 0.66 ± 0.02 |
| $\phi$ | 0.04 ± 0.005 | 0.14 ± 0.01 | 0.16 ± 0.01 | 0.16 ± 0.02 |
| $R_g$ (Å) | 780 ± 15 | 600 ± 10 | 530 ± 9 | 420 ± 7 |
| PD (%) | 0.25 ± 0.01 | 0.25 ± 0.01 | 0.25 ± 0.01 | 0.25 ± 0.01 |
| T = 30 °C | | | | |
| $\phi_{\text{eff}}$ | 0.06 | 0.19 | 0.24 | 0.34 |
| $A_1$ (cm$^{-1}$) | 680 ± 15 | 810 ± 20 | 680 ± 8 | 450 ± 4 |
| $A_2$ (cm$^{-1}$) | 13 ± 2 | 32 ± 3 | 17 ± 2 | 6.5 ± 0.4 |
| $\xi_1$ (Å) | 200 ± 4 | 200 ± 4 | 120 ± 3 | 53 ± 3 |
| $\mu_1$ (Å) | 0.85 ± 0.02 | 0.70 ± 0.01 | 0.70 ± 0.02 | 0.70 ± 0.02 |
| $\phi$ | 0.03 ± 0.002 | 0.15 ± 0.01 | 0.15 ± 0.01 | 0.17 ± 0.01 |
| $R_g$ (Å) | 740 ± 10 | 610 ± 9 | 520 ± 8 | 415 ± 7 |
| PD (%) | 0.25 ± 0.01 | 0.25 ± 0.01 | 0.25 ± 0.01 | 0.25 ± 0.01 |
| T = 40 °C | | | | |
| $\phi_{\text{eff}}$ | 0.06 | 0.19 | 0.24 | 0.34 |
| $A_1$ (cm$^{-1}$) | 1200 ± 30 | 1950 ± 40 | 2100 ± 40 | 2200 ± 50 |
| $A_2$ (cm$^{-1}$) | 17 ± 3 | 54 ± 5 | 65 ± 5 | 100 ± 8 |
| $A_3$ (cm$^{-1}$) | 0.16 ± 0.01 | 0.30 ± 0.02 | 0.50 ± 0.04 | 1.10 ± 0.06 |
| $\xi_1$ (Å) | 68 ± 2 | 70 ± 3 | 66 ± 2 | 63 ± 4 |
| $\xi_2$ (Å) | 16 ± 1 | 12 ± 1 | 14 ± 2 | 20 ± 2 |
| $\mu_1$ (Å) | 2.05 ± 0.05 | 2.0 ± 0.05 | 2.05 ± 0.06 | 2.15 ± 0.10 |
| $\mu_2$ (Å) | 0.66 ± 0.01 | 0.66 ± 0.01 | 0.66 ± 0.01 | 0.66 ± 0.01 |
| $\phi$ | 0.010 ± 0.005 | 0.030 ± 0.006 | 0.040 ± 0.005 | 0.070 ± 0.01 |
| $R_g$ (Å) | 650 ± 10 | 550 ± 10 | 510 ± 9 | 470 ± 6 |
| PD (%) | 0.21 ± 0.01 | 0.22 ± 0.02 | 0.20 ± 0.02 | 0.15 ± 0.01 |

Table S1: Parameters obtained by fitting the experimental SANS scattering intensities at T = 20, 30 and 40 °C with Eq. 6 of the main article, in which Eq. 7 (T = 20, 30 °C) or Eq. 8 (T = 40 °C) were used for $P(Q)$ and $S(Q)$ was calculated using the potential of Eq. 10 (T = 20 °C) or Eq. 11 (T = 30, 40 °C).

## SVI. EXPERIMENTAL FIT PARAMETERS: STAR POLYMER POTENTIAL

We report in Table S2 the parameters of the fits obtained from the modeling of the experimental data at T = 20 and 30 °C using Eq. 6 of the main article, in which the structure factor was calculated using the star polymer potential. The corresponding error of each parameter is also reported.

## SVII. SIMULATION FIT PARAMETERS: EFFECTIVE POTENTIAL INTERACTIONS

We report in Table S3 the parameters of the fits corresponding to the phenomenological description represented in Eq. 6 at $\alpha \geq 0.5$.

## SVIII. PHYSICAL MEANING OF THE PHENOMENOLOGICAL EXPRESSION

The potential described in the main article by Eq.(6) is just a tabulated potential that is useful to carry out the simulations. To discern the physical meaning of the various fit parameters, we discuss here an alternative representation.

As shown in Fig. S5, the calculated effective potential can also be described by the combination of a Hertzian interaction, applying to microgels in good solvent at low $T$, and an attractive potential that captures the

| T = 20 °C | | | | |
|---|---|---|---|---|
| $\phi_{\text{eff}}$ | 0.06 | 0.19 | 0.24 | 0.34 |
| $A_1$ (cm$^{-1}$) | 630 ± 20 | 580 ± 16 | 465 ± 10 | 315 ± 5 |
| $A_2$ (cm$^{-1}$) | 10 ± 1 | 35 ± 3 | 15 ± 2 | 4.5 ± 0.5 |
| $\xi_1$ (Å) | 200 ± 6 | 250 ± 8 | 140 ± 4 | 50 ± 1 |
| $\mu_1$ (Å) | 0.75 ± 0.04 | 0.66 ± 0.01 | 0.66 ± 0.01 | 0.66 ± 0.02 |
| $\phi$ | 0.06 ± 0.005 | 0.20 ± 0.02 | 0.26 ± 0.04 | 0.36 ± 0.04 |
| $R_{\text{g}}$ (Å) | 800 ± 20 | 610 ± 10 | 530 ± 8 | 415 ± 5 |
| PD (%) | 0.26 ± 0.02 | 0.25 ± 0.01 | 0.25 ± 0.01 | 0.25 ± 0.01 |
| T = 30 °C | | | | |
| $\phi_{\text{eff}}$ | 0.06 | 0.19 | 0.24 | 0.34 |
| $A_1$ (cm$^{-1}$) | 800 ± 30 | 850 ± 35 | 750 ± 20 | 510 ± 10 |
| $A_2$ (cm$^{-1}$) | 12 ± 2 | 33 ± 3 | 30 ± 2 | 6 ± 0.5 |
| $\xi_1$ (Å) | 200 ± 4 | 200 ± 2 | 175 ± 2 | 50 ± 1 |
| $\mu_1$ (Å) | 0.75 ± 0.03 | 0.73 ± 0.02 | 0.70 ± 0.04 | 0.85 ± 0.05 |
| $\phi$ | 0.06 ± 0.005 | 0.20 ± 0.02 | 0.26 ± 0.03 | 0.30 ± 0.03 |
| $R_{\text{g}}$ (Å) | 780 ± 15 | 610 ± 10 | 535 ± 7 | 410 ± 5 |
| PD (%) | 0.26 ± 0.02 | 0.25 ± 0.01 | 0.25 ± 0.01 | 0.25 ± 0.01 |

Table S2: Parameters obtained by fitting the experimental SANS scattering intensities at T = 20 and 30 °C with Eq. 6 of the main articles, in which Eq. 7 was used for $P(Q)$ and $S(Q)$ was calculated using the potential of Eq. 9.

| | $\beta V_{\alpha=0.5}$ | $\beta V_{\alpha=0.58}$ | $\beta V_{\alpha=0.7}$ |
|---|---|---|---|
| $A_0$ ($\epsilon$) | 5.76 | 6.80 | 15.01 |
| $A_1$ | 2.86 | 2.60 | 1.99 |
| $A_2$ ($\epsilon$) | -3.27 | -3.91 | 9.11 |
| $A_3$ | 6.23 | 5.60 | 2.69 |
| $A_4$ | 0.94 | 1.27 | 7.64 |
| $A_5$ | 0.58 | 0.75 | -0.63 |
| $A_6$ | 2.00 | 1.64 | 2.00 |
| $r_{cut}$ ($\sigma$) | 1.14 | 1.22 | 1.34 |
| $B_2^*$ | 3.76 | -9.28 | -126.82 |

Table S3: Parameters for the potential $\beta V_{eff}(r)$ showed in Fig. 1 in the main article, and their associated normalized second virial factor $B_2^*$.

solvophobic effects. For simplicity, we write the latter as a cosine potential. Hence, the total effective potential can be written as,

$$\beta V_{eff}(r) = \begin{cases} U\left[1-\frac{r}{r_{min}}\right]^{2.5} + U_{min}cos^2\left[\frac{\pi(r-r_{min})}{2(r_c-r_{min})}\right] & \text{if } r \le r_{min} \\ U_{min}cos^2\left[\frac{\pi(r-r_{min})}{2(r_c-r_{min})}\right] & \text{if } r_{min} < r \le r_c \\ 0 & \text{if } r > r_c \end{cases} \tag{S1}$$

where $U$ is the Hertzian strength related to the particle elasticity, $U_{min}$ and $r_{min}$ are the minimum energy and its corresponding position, respectively, that are determined by the simulations and $r_c$ is the cutoff distance when $\beta V_{eff}(r_c) = 0$. Hence, in this functional form there are much less fit parameters and the physical interpretation is clear. However, when particles become attractive, the Hertzian model starts to fail to describe the contact among attractive partcles. Indeed, we can observe in Table S4 that $U$ slightly decreases by increasing $\alpha$, i.e., copolymer microgels become softer by increasing the hydrophobicity effects. This is due to the fact that Hertzian model does not properly capture excluded volume when particles are attractive. To avoid this, we adopted a functional form in which the low-distance repulsion is represented by a generalized Lennard-Jones shape, which contains the Hertzian.

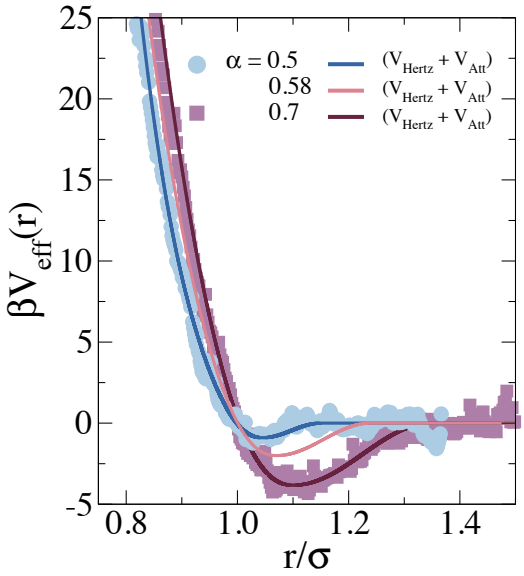


Figure S5: Effective potential interaction $\beta V_{eff}(r)$ obtained by umbrella sampling (symbols), and their corresponding physical interpretation ($V_{Hertz} + V_{Att}$.) The effective interaction at $\alpha = 0.58$ is obtained by interpolation.

| | $U$ ($\epsilon$) | $U_{min}$ ($\epsilon$) | $r_{min}$ ($\sigma$) | $r_c$ ($\sigma$) | $B_2^*$ |
|---|---|---|---|---|---|
| $\alpha = 0.5$ | 1300 | -0.9 | 1.045 | 1.15 | 5.69 |
| $\alpha = 0.58$ | 1200 | -2 | 1.07 | 1.24 | -1.98 |
| $\alpha = 0.7$ | 1145 | -3.83 | 1.1 | 1.35 | -84.73 |

Table S4: Parameters of the potential $\beta V_{eff}(r)$ corresponding to Eq. S1 and showed in Fig. S5, and their associated normalized second virial factor $B_2^*$.

By comparing the two potential representations, no main differences arise, as shown in Fig. S5. Also, the normalized second virial coefficients of the two potentials are quite similar and they give nearly identical results for the static and dynamic properties of the system with increasing packing fraction.

## SIX. POLYDISPERSITY EFFECTS ON THE STATIC STRUCTURE FACTOR

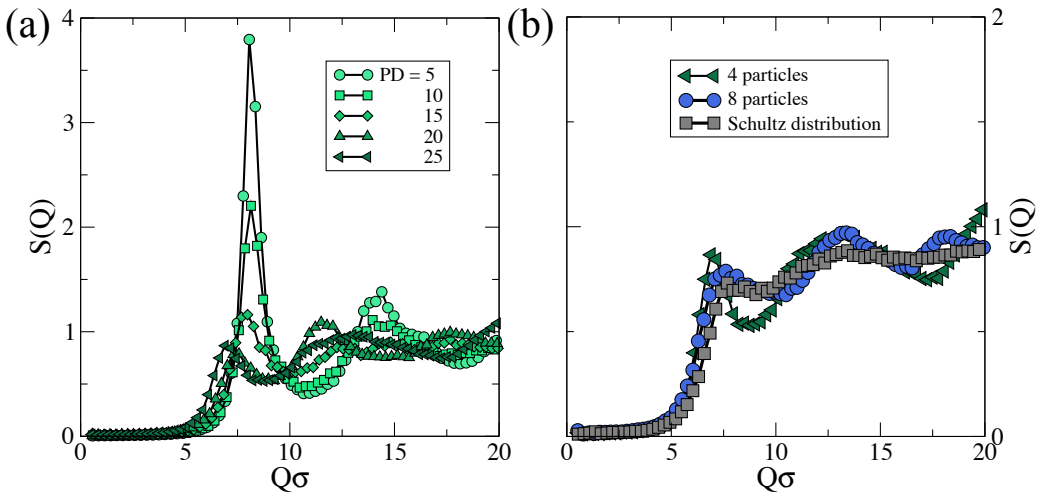


Figure S6: Static structure factor $S(Q)$ of a polydisperse system interacting with the Hertzian model at $\phi = 0.80$. (a) $S(Q)$ as a function of the polydispersity $PD$, introduced by considering 4 populations of particles with different diameters. (b) $S(Q)$ with $PD = 25\%$ for different ways of calculating the distributions (4 and 8 populations, Schulz).

As shown in Fig. 6 in the main article, the main peak of $S(Q)$ goes below 1 by increasing $\phi$ for the Hertzian model, corresponding to $\alpha = 0.0$. It is well-known that the Hertzian model exhibits a reentrant behavior with increasing $\phi$ but the main peak of $S(Q)$ for a monodisperse system does not go below 1. In Fig. S6(a) we plot $S(Q)$ at $\phi = 0.80$ for the Hertzian model and various values of polydispersity PD, increasing from 5% to 25%, when we use only 4 sizes of the particles. It can be seen that the main peak decreases its height with increasing PD, shifting to lower values of $Q\sigma$. For PD $> 20\%$, its maximum is below 1.

Additionally in Fig. S6(b), we then fixed the polydispersity at $PD = 25\%$, but changed the size distribution from using only 4 sizes, to 8 sizes to a continuous Schultz distribution, that is the one used in the main article. From this, we observe how increasing the diversity of particles with different diameters makes the first peak even lower and also slightly shifts it towards larger $Q\sigma$ values.

## SX. CORE-CORONA EFFECTS IN COMPOSITE MICROGELS

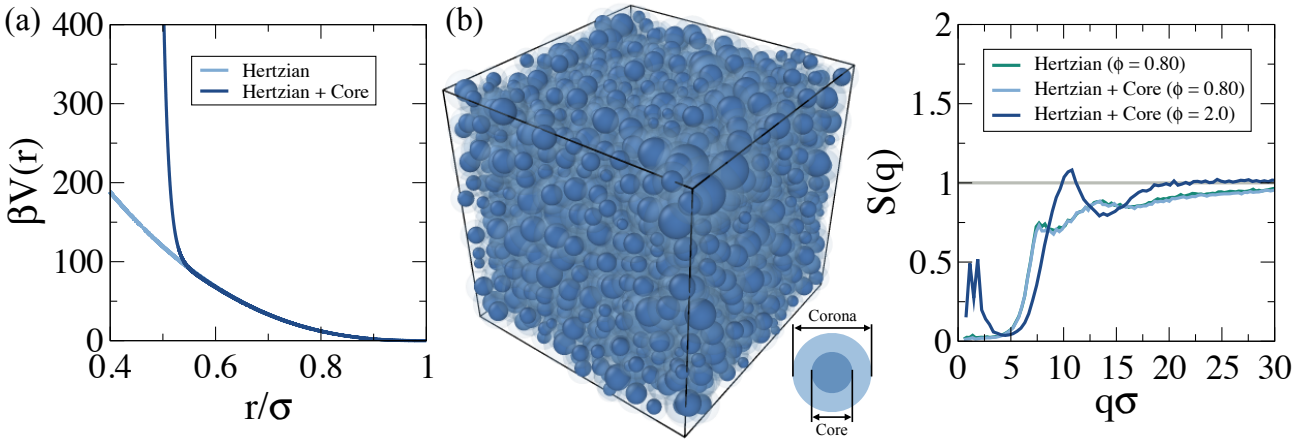


Figure S7: (a) Effective potential interaction describing the structure factor from SANS data, and the effective interaction including the presence of a core. (b) Snapshots of the system at $T = 30°$, and the static structure factor $S(Q)$ considering Hertzian and Hertzian+Core interaction at $\phi = 0.80$, and the Hertzian+Core interaction at $\phi = 2.0$.

Fig. S7 proves that in the range of packing fractions discussed in the main text, the core effects are negligible. The diameter of the core was estimated by the SANS measurements which indicate that the diameters corresponding to the composite microgel and internal core are 160 nm and 90 nm, respectively. Thus, we fixed an effective core in our simulations of size $\sigma_{core} = 0.55\sigma_m$, being the effective potential interaction expressed as $V_{CC}(r) = V_H + V_{Core}$, see Fig. S7(a). Here, $V_H$ represents the effective potential interaction described in Eq. 10, whereas $V_{Core}$ mimics the core, defined as

$$\beta V_{core}(r) = 4\epsilon \left[ \left( \frac{0.55\sigma_m}{r} \right)^{48} - \left( \frac{0.55\sigma_m}{r} \right)^{12} \right]. \tag{S2}$$

Fig. S7(b) illustrates the core-core contact that induces a peak in the $S(Q)$ at $\phi = 2.0$. Finally, we observe that the core effects are shielded in the range of packing fractions explored in the main, i.e. $\phi \leq 0.80$, as shown by the overlap of $S(Q)$ computed for both descriptions.